Springer

Acta Mechanica Sinica

CrossMark click for updates

• RESEARCH PAPER •

Acta Mech. Sin., Vol. 39, 123168 (2023)
https://doi.org/10.1007/s10409-023-23168-x

Non-resonant elastic metamaterials for broadband perfect mode conversion and negative reflection

Zhou Hu[1], Mingye Zheng[2], Kaijun Yi[1*], Rui Zhu[1*], and Gengkai Hu[1]

[1] *School of Aerospace Engineering, Beijing Institute of Technology, Beijing 100081, China;*
[2] *Beijing Institute of Radio Measurement, Beijing 100854, China*

Received April 7, 2023; accepted June 2, 2023; published online August 25, 2023

Reflection control of elastic wave is of great importance. Recently, reflective metasurfaces governed by the generalized Snell's law offer a new degree of freedom to control the direction as well as the polarization of the reflected elastic waves. However, the underlining mechanism of the reflective metasurfaces is frequency-dependent, which significantly limits their practical applications. Here, we propose frequency-independent metamaterials called singly polarized solids (SPSs) for broadband reflection control of elastic waves. With the engineered SPSs, perfect mode conversion (PMC) and switching between positive reflection (PR) and negative reflection (NR) are achieved. Our work opens an approach to control the reflected elastic waves in a broad frequency range, and could find potential applications in structural health monitoring, nondestructive detection, and elastic wave devices.

Non-resonant elastic metamaterials, Mode conversion, Negative reflection

Citation: Z. Hu, M. Zheng, K. Yi, R. Zhu, and G. Hu, Non-resonant elastic metamaterials for broadband perfect mode conversion and negative reflection, Acta Mech. Sin. 39, 123168 (2023), https://doi.org/10.1007/s10409-023-23168-x

1. Introduction

Reflection is a fundamental wave phenomenon which usually occurs at the discontinuous interfaces, and is of great importance in various applications, such as communications, imaging, nondestructive evaluation, wave mitigation [1-6]. Wave reflection obeys the well-known Snell's law, which results in the same incidence and reflection angles in fluids, but leads to additional reflected transverse wave in isotropic solids (Fig. 1a). Recently, the generalized Snell's law (GSL) was proposed, which stated that by introducing abrupt phase shifts, an incident wave could be reflected at any specific direction, beyond what the usual reflection law predicted [7]. Since then, metasurfaces with particularly designed unit cells based on the GSL [8,9], have been studied extensively to realize the phase gradient for various exotic sound wave reflection phenomena, such as conversion from propagating waves to surface waves [10,11], focusing [12,13], negative reflection (NR) [14,15], and even retroreflection [16,17]. Different from sound waves with a single polarization characteristic, elastic waves are characterized by multiple polarization characteristics and the inherent mode coupling resulting from the tensorial nature of elasticity [18]. Therefore, both direction and polarization of elastic waves involved in the reflection need to be considered. Kim et al. [19] extended the concept of metasurfaces to elastodynamics and designed an elastic metasurface consisted of slender and straight beam-type unit cells, where a sufficiently large phase gradient was introduced so that an incident longitudinal (L) wave could be perfectly converted into a reflected transverse (T) wave. This so-called transmodal elastic metasurface can make perfect mode conversion (PMC) from L to T waves at specific frequencies. By designing the elastic metasurface with an extremally large phase gradient, the incident L wave can even be converted into a surface wave, which is entrapped by the local resonator and eventually damped out,

*Corresponding authors. E-mail addresses: kaijun.yi@bit.edu.cn (Kaijun Yi); ruizhu@bit.edu.cn (Rui Zhu)
Executive Editor: Guoliang Huang

leading to zero reflection [20]. However, unwanted multiple modes are often generated when the periodicity of the metasurface is comparable to the wavelength, leading to poor efficiency [21]. More recently, by solving the inverse problems with optimization methods, metagratings with appropriate geometry of unit cells are designed, which can selectively suppress superfluous scattered modes and therefore, lead to high efficiency anomalous reflection [22], reflection-type beam splitting and near PMC [23,24]. Although metasurfaces and metagratings offer unconventional ways to manipulate both polarization and direction of the reflected elastic waves, the fundamental operating mechanism based on GSL is frequency-dependent. Therefore, there is a high demand to find broadband wave mechanism beyond GSL.

In fact, both polarization and direction of the reflected elastic waves can be steered by harnessing the anisotropic elasticity of the propagating material which possesses particular frequency-independent equi-frequency curves (EFCs). For example, when the incident elastic waves hit the free boundary of some anisotropic nature materials at certain angles, PMC can be observed [25]. However, controlling both polarization and direction at will is very difficult if not impossible with only nature materials. To this end, Lee et al. [26] proposed a well-designed elastic metamaterial consisted of off-centered, double-slit unit cells. By tuning the geometrical size of the unit cell, the elastic metamaterial can exhibit unusual polarization transition from L to T waves in one of its EFCs which can lead to PMC in a broad frequency range. Due to the direction of L or T wave predicted by the specific EFC is parallel to the principal direction of the metamaterial, it fails to steer the direction of the reflected wave going in other desired directions. Ahn et al. [27] developed a topology optimization approach to design elastic metamaterials with desired EFCs and wave modes so that the mode conversion and direction manipulation can be simultaneously achieved at a target frequency, but the design of elastic metamaterials with both specific EFCs and wave modes over broadband efficiency has not been realized. Most recently, Zheng et al. [28,29] proposed the concept of singly polarized solid (SPS) that supports only one polarization along all directions. As a result, the inherent mode decoupling and broadband efficiency of SPSs open a new gate for efficient reflection control of both elastic wave's polarization and direction.

In this work, by engineering the EFC of the elastic metamaterial, we realize the simultaneous manipulation of the polarization and direction of elastic waves over a wide frequency range through wave reflections. First, wave reflections in semi-infinite SPSs are theoretically analyzed based on their frequency-independent EFC. The PMC between L wave and T wave can be achieved, while a positive reflection (PR) (Fig. 1b) or a NR (Fig. 1c) can be generated by leveraging the anisotropic stiffness. Then, a non-resonant microstructure for a SPS supporting singly polarized elastic wave is designed and verified via the EFCs over a broadband frequency range. Finally, a time domain simulation using the designed non-resonant metamaterial verifies the PMC with NR from L to T wave.

2. Broadband polarization and direction control of elastic waves in SPSs through wave reflections

To simultaneously steer the polarization and direction of elastic waves at a free boundary, we assume that there exists a type of frequency-independent metamaterials in which an L wave can be perfectly converted into a reflected T wave either going in the specular direction indicating the PR occurs (Fig. 1b) or going back in the same side of the incidence indicating the NR occurs (Fig. 1c). To find this type of metamaterials, we start with the analysis on EFCs of the elasticity. For an isotropic solid medium, there always exists two EFCs indicating it supports two wave modes (L and T waves). This is the reason that incomplete mode conversion

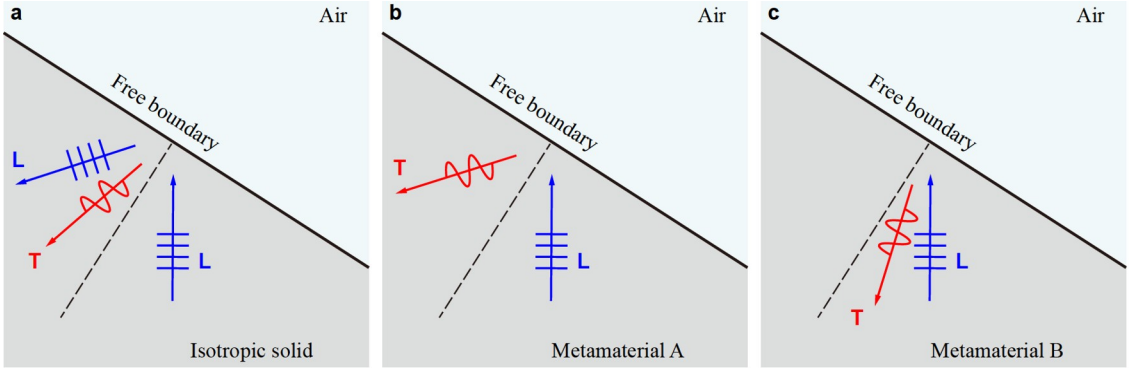

Figure 1 Schematic of the reflection of elastic waves in three semi-infinite elastic media. **a** Imperfect mode conversions with all PRs in a semi-infinite isotropic solid. **b** PMC with the PR in a semi-infinite metamaterial A. **c** PMC with NR in a semi-infinite metamaterial B. L and T represent longitudinal and transverse waves, respectively.

can be observed when an incident L wave impinges on a free boundary as shown in Fig. 2a. In order to achieve broadband PMC through the wave reflection, the metamaterials need to be engineered to achieve: (1) only one EFC exists at any frequency so that broadband mode decoupling can be realized; (2) polarization transition from L to T waves is supported in the only one EFC so that mode conversion can be realized through the wave reflection. According to the previous study [28,29], SPSs, which support only one wave mode, are good candidates. Next, we will briefly review the dynamic properties of SPSs and find the particular SPSs that can enable PMC through the wave reflection.

The elastic matrix of a SPS under the principal directions (the x and y directions) can be expressed as

$$\mathbf{C}=\begin{bmatrix} C_{11} & C_{12} & 0 \\ C_{12} & C_{22} & 0 \\ 0 & 0 & 0 \end{bmatrix},\ C_{12}^2 = C_{11}C_{22}, \tag{1}$$

and the wave propagation in the SPS is governed by the equation of motion as

$$\begin{bmatrix} C_{11}k_x^2 & C_{12}k_xk_y \\ C_{12}k_xk_y & C_{22}k_y^2 \end{bmatrix}\begin{bmatrix} v_x \\ v_y \end{bmatrix} = \rho\omega^2\begin{bmatrix} v_x \\ v_y \end{bmatrix}, \tag{2}$$

where k_x and k_y are the two components of the wavevector, v_x and v_y are the two components of the particle velocity vector, ρ denotes the mass density, and ω denotes the circular frequency. As a result, the wave dispersion relation of the SPS can be obtained as

$$\rho\omega^2 = C_{11}k_x^2 + C_{22}k_y^2. \tag{3}$$

It is confirmed that there is only one EFC for the SPS at any frequency.

Moreover, the wave polarization characteristic of the SPS can be obtained as

$$\tan\theta_{\mathrm{v}} = \frac{v_y}{v_x} = \frac{C_{12}}{C_{11}}\tan\theta_{\mathrm{k}}, \tag{4}$$

where θ_{k} represents the wavevector orientation. Then, we define the polarization angle θ_{p} as

$$\theta_{\mathrm{p}} = \left|\theta_{\mathrm{v}} - \theta_{\mathrm{k}}\right| = \tan^{-1}\left|\frac{(C_{11}-C_{12})\tan\theta_{\mathrm{k}}}{C_{11}+C_{12}\tan^2\theta_{\mathrm{k}}}\right|, \tag{5}$$

where $\theta_{\mathrm{p}} = 0°$ and 90° correspond to the L wave and T wave, respectively. From Eq. (5), it can be found that $\theta_{\mathrm{p}} = 0°$ if $\tan\theta_{\mathrm{k}} = 0$, indicating that the L wave is supported in these principal directions. While there is only one solution for $\theta_{\mathrm{p}} = 90°$ that is

$$\tan^2\theta_{\mathrm{k}} = -\frac{C_{11}}{C_{12}}, \tag{6}$$

which suggests $C_{12} < 0$. From Eq. (1), it can be found that the SPSs with

$$C_{12} = -\sqrt{C_{11}C_{22}} \tag{7}$$

is the only solution, and the polarization angle can be re-

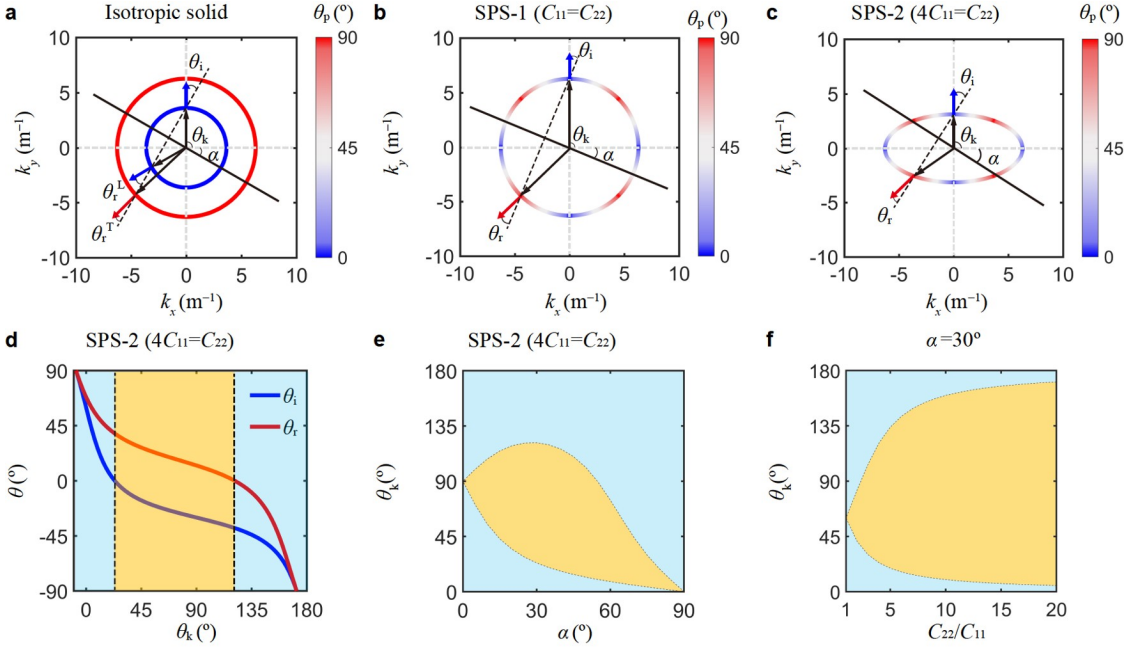

Figure 2 EFC analysis for the polarization and direction of the wave reflections in different elastic media. Reflections of elastic waves **a** in an isotropic solid, **b** in the SPS with $C_{11} = C_{22}$ and $\alpha = 22.5°$ (indicated as SPS-1), and **c** in the SPS with $4C_{11} = C_{22}$ and $\alpha = 32.4°$ (indicated as SPS-2). θ_{p} represents the polarization angle. α represents the angle between the free boundary and the principal axis, which is the key to achieve PMC. θ_{k} denotes the direction of the wavevector. θ_{i} and θ_{r} represent the incident and reflected angles of the power flow with respect to the free boundary normal, respectively. **d** Directions of the power flows of the incident wave (blue line) and the reflection wave (red line) as functions of wavevector directions in the SPS-2. **e** The PR and NR regions in the SPS-2 as a function of the angle α. **f** The PR and NR regions as a function of the ratio C_{22}/C_{11}.

written as

$$\tan\theta_p = \left| \frac{\left(\sqrt{C_{11}} + \sqrt{C_{22}}\right)\tan\theta_k}{\sqrt{C_{11}} - \sqrt{C_{22}}\tan^2\theta_k} \right|. \tag{8}$$

Equation (8) confirms that as the wavevector direction θ_k changes, the polarization angle θ_p continuously varies from 0° to 90°, which means, in these principal directions ($\tan\theta_k = 0$) only L waves are supported in the SPS, and in other directions ($\tan\theta_k = \sqrt[4]{C_{11}/C_{22}}$) only T waves are allowed. Therefore, the SPSs satisfying Eq. (7) enable broadband PMC through the wave reflection at free boundaries with delicately chosen azimuths.

To demonstrate the above statement, Fig. 2b shows a circular EFC of the SPS with $C_{11} = C_{22} = -C_{12}$ (indicated as SPS-1). It can be found that all possible polarization characteristics can be supported in SPS-1 as θ_k changes. Specifically, in some directions ($\theta_k = 45°, 135°, 225°, 315°$), only T wave is supported, and in these principal directions ($\theta_k = 0°, 90°, 180°, 270°$), only L wave is supported. As a result, a free boundary at an angle of $\alpha = 22.5°$ to the principal axis (the x axis) of the SPS-1 is designed based on the Snell's law (see Appendix). When a L wave impinges on the boundary from the direction $\theta_k = 90°$, it will be fully converted to a T wave propagating along the direction $\theta_k = 225°$. Conversely, when a T wave impinges on the boundary from the direction $\theta_k = 225°$, it will be fully converted to a L wave propagating along the direction $\theta_k = 90°$. Therefore, the PMC between L and T waves can be achieved, but it is always accompanied by a PR.

To steer the direction of the reflected elastic wave, we consider the anisotropic stiffness of the SPSs enabling to deflect the direction of power flows away from that of wavevectors. Since the direction of power flows in a SPS is parallel to the normal direction of its EFC, the deflection of the energy flow can be achieved by changing the EFC from a circle to an ellipse. An elliptical EFC of the SPS with $4C_{11} = C_{22}$ (indicated as SPS-2) is shown in Fig. 2c, and a special area (the yellow shaded area) exists where the power flows of the incident and reflected waves are on the same side of the free boundary normal, indicating NR occurs. More importantly, all possible polarization characteristics are supported in the SPS-2, therefore, PMC can also be achieved through the wave reflection.

To quantitatively evaluate the NR region, directions of the power flows with respect to the free boundary normal of the SPS-2 are analyzed based on Eqs. (A2) and (A4) in Appendix. Directions of the power flows of both incident and reflected waves, θ_i and θ_r, as functions of wavevector directions in the SPS-2 are shown in Fig. 2d. NR region (the yellow shaded area) and PR region (the light blue shaded area) are also illustrated, which is consistent with the schematic diagram of NR and PR regions in Fig. 2c. Moreover, the effect of α on the NR region is studied, as shown in Fig. 2d. Two conclusions can be drawn: (1) when $\alpha = 0°$ or 90°, indicating the free boundary is parallel to the principal axis of the SPS-2, there is no NR, (2) the NR region increases first and then decreases as α increases.

In order to enlarge the NR region, optimization of SPS's properties is performed. Since SPS only has two independent elastic coefficients (C_{11} and C_{22}), the ratio C_{22}/C_{11}, representing the stiffness anisotropy, can be used as the only optimization variable. Figure 2f shows that the larger the ratio C_{22}/C_{11} is, the larger the NR region is. It should be noted that although we consider SPSs with $C_{22}/C_{11} > 1$, SPSs with $C_{22}/C_{11} < 1$ can be derived by rotating the principal axis of the SPS with $C_{22}/C_{11} > 1$ by 90°.

Wave simulations are conducted to verify the PMC with either PR or NR in two different SPSs. The homogeneous model with a tilted free boundary deviating from the principal axis (or x-axis) by an angle of α is constructed in the commercial software COMSOL Solid Mechanics module, where the principal axis of the homogeneous SPS coincides with the global coordinate system. Perfect matched layers are applied to all other boundaries except for the tilted free boundary to avoid the unwanted boundary reflection. A harmonic L wave Gaussian beam (blue arrows in Fig. 3a) with 30 kHz is launched from the bottom-right of the SPS, travelling to the tilted free boundary. Figure 3b and c shows the amplitudes of the in-plane displacement fields in the

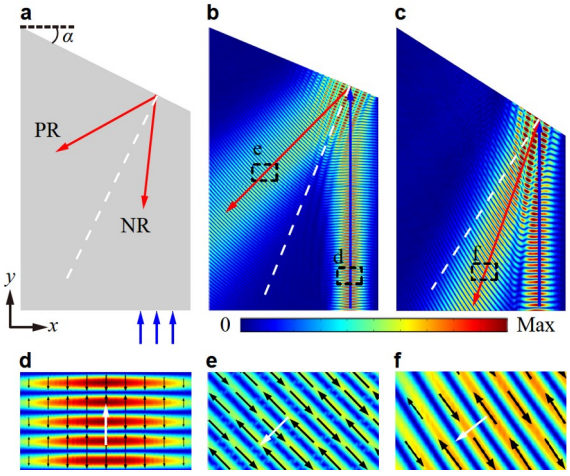

Figure 3 Simulation results of PMC with either PR or NR in SPSs. **a** A schematic diagram for the simulation. Blue and red arrows represent the incident and reflected waves, respectively. The reflected wave going in the upper side (or bottom side) with respect to the boundary normal (white dashed line) is defined as PR (or NR). Amplitudes of the in-plane displacement fields at 30 kHz in **b** the SPS-1 ($C_{11} = C_{22}$) and **c** the SPS-2 ($4C_{11} = C_{22}$). **d** The zoomed incident wave field in SPS-1, **e** the reflected wave field in SPS-1 and **f** the reflected wave field in SPS-2. White and black arrows represent the wavevector direction and the polarization characteristic, respectively.

SPS-1 ($C_{11} = C_{22}$, $\alpha = 22.5°$) and the SPS-2 ($4C_{11} = C_{22}$, $\alpha = 32.4°$), respectively. First, there is only one reflected wave in both cases. Second, polarization characteristics of the partially zoomed incident and reflected wave fields in Fig. 3d and f show that the polarization direction (black arrow) is parallel to the wavevector direction (white arrow) for the incident wave (L polarized), while the polarization direction is perpendicular to the wavevector direction for the reflected wave (T polarized). Moreover, PR in SPS-1 and NR in SPS-2 can be directly observed, and further calculations of the angle between the power flows of the reflected wave and the boundary normal (white dashed line) showing that $\theta_r = +22.5°$ in SPS-1 and $\theta_r = -13°$ in SPS-2 also demonstrate this point.

3. Design of non-resonance elastic metamaterial and realization of PMC with NR

Previous studies [28,29] have demonstrated that the concave hexagon configuration with is a good candidate microstructure for SPSs. Here, we choose a concave hexagon configuration with attached mass block (Fig. 4a) as the basic configuration of SPS. Figure 4b shows a representative unit cell of the metamaterial with seven geometrical parameters (a, b, w, h, t, w_1, h_1) and its finite element (FE) model. a and b are two lattice constants, w and h are the width and height of the attached mass block, and t is the thickness of the horizontal beam, which contributes to the shear effect of the microstructure [28-30]. In this study, we first specify a sufficiently small value of $t = 0.25$ mm and define $w_1 = \frac{w}{2} + \frac{l_0 t}{b} + \frac{\sqrt{4l_0^2 - b^2}}{4b}(b - 2h)$, $h_1 = \frac{b - h - t}{2}$, where $l_0 = 20t = 5$ mm is a characteristic length. Therefore, the effective material properties are determined by four dimensionless parameters: $a' = \frac{a}{l_0}$, $b' = \frac{b}{l_0}$, $w' = \frac{w}{l_0}$, $h' = \frac{h}{l_0}$. Since we concern the frequency-independent properties of the elastic metamaterial, its effective mass density and the effective elastic matrix can be extracted based on a numerical-based effective medium method [30]. Note that the larger the characteristic length, the smaller the effective shear modulus of the metamaterial.

Second, by sweeping the four dimensionless parameters, we can obtain many different designs with different effective material properties. Since the larger the ratio C_{22}/C_{11} the easier the realization of NR, we choose an aluminum-based ($\rho_0 = 2700\ \mathrm{kg \cdot m^{-3}}$, $C_{11}^0 = 102.2$ GPa, $C_{66}^0 = 25.9$ GPa) metamaterial design with $a = 4.63$ mm, $b = 9.85$ mm, $t = 0.25$ mm, $w = 2.5$ mm, $h = 8.92$ mm, $w_1 = 3.78$ mm, $h_1 = 0.34$ mm, and its effective material parameters are $\rho = 710.8\ \mathrm{kg \cdot m^{-3}}$, $C_{11} = 0.3188$ GPa, $C_{22} = 8.8155$ GPa, $C_{12} = -1.5039$ GPa, and $C_{66} = 0.0036$ GPa, where $C_{11}/C_{22} = 27.65$ implies strong anisotropy of modulus.

To illustrate the broadband properties of the design metamaterial, we calculate the band structures with its FE model. As shown in Fig. 5a, only one longitudinal band structure (red solid line) in the frequency range of 20-40 kHz (shaded region), which is linear, implies that the metamaterial with detail microstructures is non-resonant. Comparing with the resonance-based metamaterials which operate near their resonant frequencies, the designed metamaterial in this manuscript is broadband. We also define a relative frequency bandwidth as

$$F_B = \frac{2(f_H - f_L)}{f_H + f_L}, \tag{9}$$

where f_L and f_H represent the lower and upper boundaries of the frequency range (shaded region in Fig. 5a). The designed metamaterial has a relative frequency bandwidth of $F_B = 0.67$, which is broadband. It should be noted that the frequency range of 0-40 kHz is achievable when the shear effect of the unit cell completely disappears.

To show the frequency-independent properties of the metamaterial, we compare the longitudinal band structure of the FE model with that of the corresponding homogenized model. Due to the homogenized model is considered frequency-independent, and the longitudinal band structure of

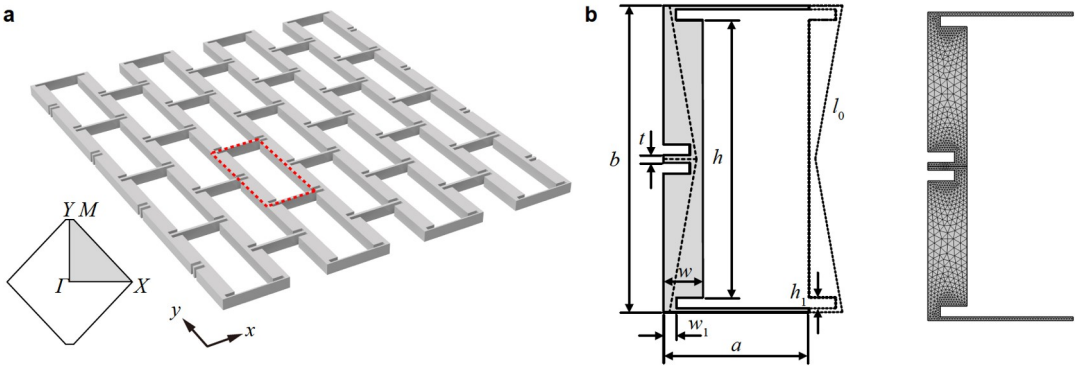

Figure 4 **a** Microstructure composed of a concave hexagon configuration with the attach mass. **b** A representative unit cell and its FE model.

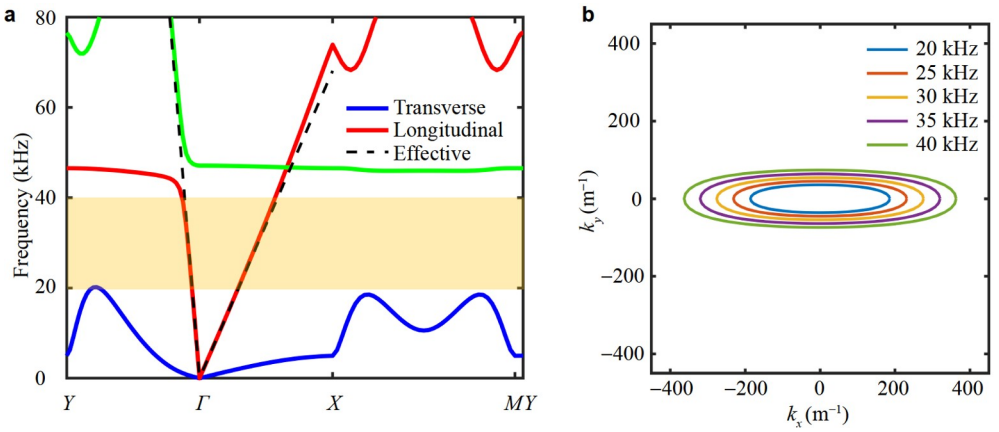

Figure 5 **a** Band structures of the designed elastic metamaterial. **b** EFCs of the designed metamaterial in a frequency range of 20-40 kHz.

the homogenized model is linear. The slope of the band structure along ΓX is $\sqrt{C_{11}/\rho}/(2\pi)$ and along ΓY is $\sqrt{C_{22}/\rho}/(2\pi)$. Both band structures fit well in the frequency range of 0-40 kHz, indicating that the designed metamaterial is frequency-independent.

We also show EFCs of the designed metamaterial in the frequency range of 20-40 kHz in Fig. 5b. Only one EFC exists at a fixed frequency implying the singly polarized characteristic, and the elliptical EFC suggests anisotropic wave behaviors. Of note is the fact that the EFC varies proportionally with the frequency, indicating the metamaterial is nondispersive in this broadband frequency range.

Finally, a transient wave propagation in a metamaterial sample consisting of about 5000 unit cells is simulated, as shown in Fig. 6. The tilted free boundary is constructed by removing upper-right corner, which deviates from the principal axis (or the x-axis) by 46.7° (Fig. 6a). Displacement excitation along the vertical direction (y direction) is applied to the central part of the bottom side of the metamaterial sample to stimulate a plane L incident wave. A tone burst signal $U_y(t) = A_0\left[1-\cos\left(\frac{2\pi f_0 t}{3.5}\right)\right]\sin(2\pi f_0 t)$ is chosen to excite the motion, where f_0 is the central frequency. The waveform with $f_0 = 30$ kHz and the corresponding frequency spectrum are shown in Fig. 6b. The frequency bandwidth (−3 dB bandwidth) of the signal is 12.4 kHz from 23.8 kHz to 36.2 kHz, in which the metamaterial is nondispersive. Figure 6c shows the process of an incident L wave propagating in the metamaterial sample, impinging on and reflected from the tilted free boundary. First, when t = 0.16 ms, a L wave with large wavelength travels towards the tilted boundary. Then, when t = 0.22 ms, the L wave impinges on the tilted boundary. Finally, the reflected wave with a small wavelength travels away from the free boundary, indicating the wave mode is converted. For comparison, the simulation results with the corresponding homogenized model are shown in Fig. 6d, and both results agree well. Moreover, the polarization characteristics as well as wavelengths of the incident wave and the reflected wave in the bottom column of Fig. 6d clearly demonstrate the PMC.

To determine the direction of the reflected wave, we evaluated the direction of Poynting vectors $\mathbf{P} = -\mathbf{v}\cdot\tilde{\sigma}$, where $\mathbf{v}$ is the particle velocity vector and $\tilde{\sigma}$ is the stress field tensor. Figure 6e shows the power flows at 0.16 ms and at 0.28 ms. It can be visualized that both the incident and the reflected power flows are on the same side with respect to the tilted free boundary normal, indicating the NR occurs.

4. Conclusion

In summary, we propose a non-resonant elastic metamaterial characterized by only supporting one wave mode along any direction. The singly polarized characteristic of this metamaterial enables the uncoupling of different wave modes. PMC between two wave modes is achieved through wave reflection. In addition, by tuning the stiffness anisotropy in two principal directions, PR and NR can also be realized. A non-resonant elastic microstructure is designed and EFC calculations illustrate the singly polarized characteristic in a broadband frequency range from 20 kHz to 40 kHz. Finally, a time-domain simulation successfully validates the PMC with NR from L wave to T wave in the designed elastic metamaterial. We believe that the proposed non-resonant elastic metamaterials offer new possibilities for the full control of elastic waves and should be beneficial for the development of elastic wave devices. Moreover, the broadband feature of the non-resonant elastic metamaterial shows promise in practical applications.

Appendix: Wave propagation in a semi-infinite SPS

According to the wave dispersion relationship of the SPS, the phase velocity can be derived as

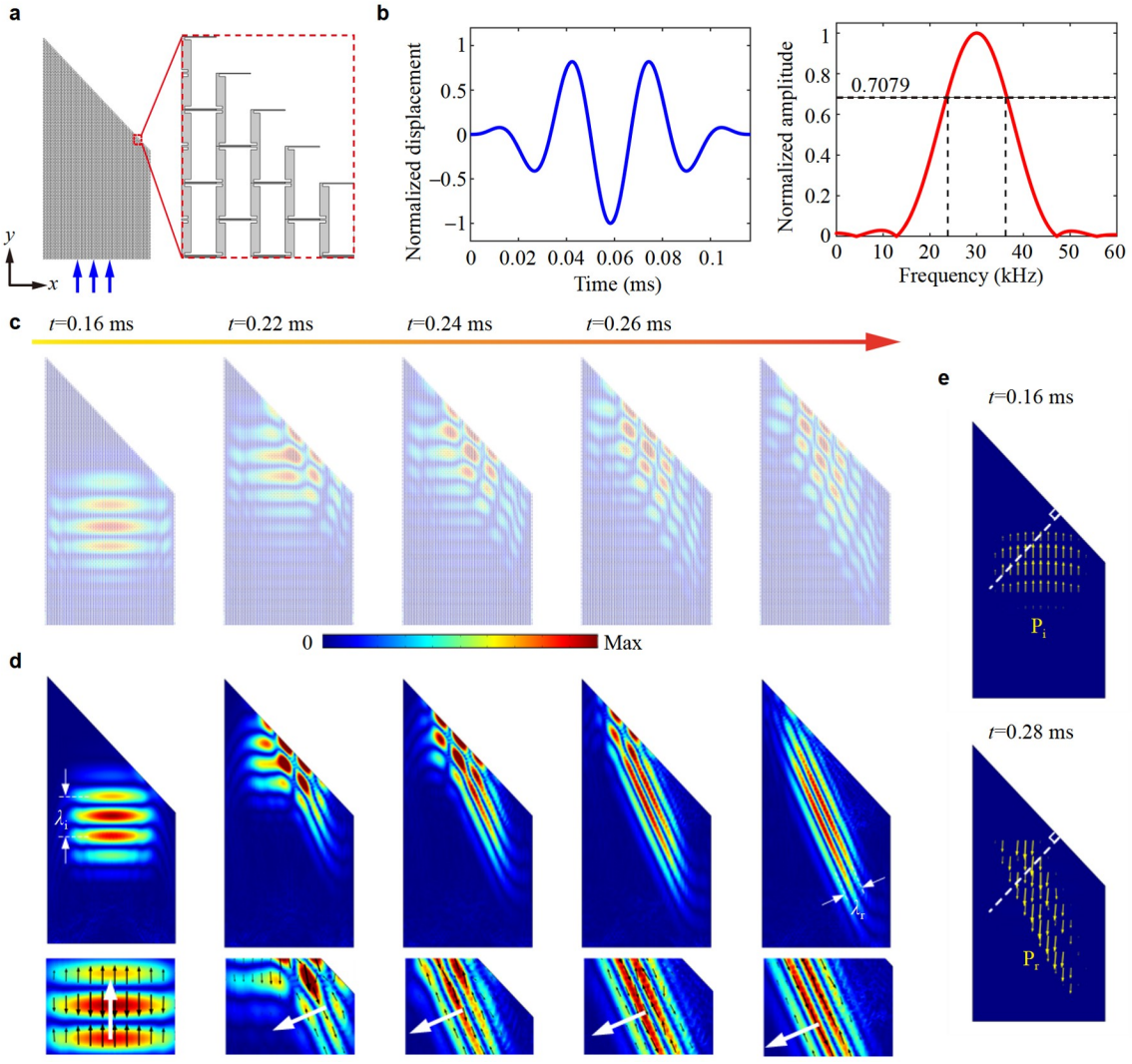

Figure 6 Numerical validation of PMC with NR in the metamaterial with designed microstructures. **a** The designed metamaterial sample used for the transient simulation. **b** Waveform (left) and frequency spectrum (right) of the tone burst signal. **c**, **d** Simulation results of normalized displacement field **c** with the metamaterial sample and **d** with the corresponding homogenized sample. λ_i and λ_r represent wavelengths of incident and reflected waves, respectively. Zoomed wave fields (bottom column) show the polarization characteristics (black arrows) and the wavevector direction (white arrows). **e** The power flows of the incident and reflected waves described by two Poynting vectors P_i and P_r, respectively.

$$V_{\mathrm{ph}} = \frac{\omega}{k} = \sqrt{\frac{C_{11}+C_{22}\tan^2\theta_{\mathrm{k}}}{\rho\left(1+\tan^2\theta_{\mathrm{k}}\right)}}, \tag{A1}$$

where k is the wavenumber, and the direction of the power flow denoted as θ_{g} can be described by the group velocity

$$\tan\theta_{\mathrm{g}} = \frac{\partial\omega}{\partial k_y} \Big/ \frac{\partial\omega}{\partial k_x} = \frac{C_{22}}{C_{11}}\tan\theta_{\mathrm{k}}. \tag{A2}$$

In a semi-infinite SPS with a free boundary deviating from the principal axis by an angle of α, the reflection of a plane elastic wave can be determined based on the Snell's law:

$$\frac{\cos\left(\theta_{\mathrm{ki}}+\alpha\right)}{V_{\mathrm{ph}}^{\mathrm{i}}} = \frac{\cos\left(\theta_{\mathrm{kr}}+\alpha\right)}{V_{\mathrm{ph}}^{\mathrm{r}}}, \tag{A3}$$

where θ_{ki} and $V_{\mathrm{ph}}^{\mathrm{i}}$ represent the wavevector orientation and phase velocity of the incident wave; θ_{kr} and $V_{\mathrm{ph}}^{\mathrm{r}}$ represent the wavevector orientation and phase velocity of the reflected wave. To achieve complete L-to-T conversion through reflection in a SPS, the angle α can be determined from Eq. (A3). In addition, the direction of the power flows of the incident and reflected waves can be derived from Eq. (A2). To identify the NR region, an angle denoting the power flow with respect to the free boundary normal is defined as

$$\theta = 90 - \left(\theta_{\mathrm{g}} + \alpha\right). \tag{A4}$$

If $\theta_{\mathrm{i}}\theta_{\mathrm{r}} < 0$, the NR occurs, otherwise the PR occurs.

Conflict of interest *On behalf of all authors, the corresponding author states that there is no conflict of interest.*

Author contributions *Zhou Hu and Rui Zhu designed the research. Zhou Hu and Mingye Zheng performed the theoretical analysis and the numerical simulations. Kaijun Yi and Rui Zhu supervised the research. All authors wrote the manuscript.*

Acknowledgements *This work was supported by the National Key R&D Program of China (Grant No. 2021YFE0110900), and the National Natural Science Foundation of China (Grant Nos. U22B2078, 11991033, and 12202052).*

1 L. Novotny, and B. Hecht, Principles of Nano-Optics (Cambridge Univ. Press, New York, 2006).
2 H. Medwin, and S. C. Clay, Fundamentals of Acoustical Oceanography (Academic press, San Diego, 1997).
3 P. J. White, G. T. Clement, and K. Hynynen, Longitudinal and shear mode ultrasound propagation in human skull bone, Ultrasound Med. Biol. **32**, 1085 (2006).
4 R. Zhu, G. L. Huang, and F. G. Yuan, Fast damage imaging using the time-reversal technique in the frequency-wavenumber domain, Smart Mater. Struct. **22**, 075028 (2013).
5 F. Yang, Z. Li, Z. Zhuang, and Z. Liu, Evaluating the blast mitigation performance of hard/soft composite structures through field explosion experiment and numerical analysis, Acta Mech. Sin. **38**, 121238 (2022).
6 Q. Wu, H. Qian, Y. Chen, and G. Huang, Dynamic phononic crystals with spatially and temporally modulated circuit networks, Acta Mech. Sin. **39**, 723007 (2023).
7 N. Yu, P. Genevet, M. A. Kats, F. Aieta, J. P. Tetienne, F. Capasso, and Z. Gaburro, Light propagation with phase discontinuities: Generalized laws of reflection and refraction, Science **334**, 333 (2011).
8 B. Assouar, B. Liang, Y. Wu, Y. Li, J. C. Cheng, and Y. Jing, Acoustic metasurfaces, Nat. Rev. Mater. **3**, 460 (2018).
9 A. L. Chen, Y. S. Wang, Y. F. Wang, H. T. Zhou, and S. M. Yuan, Design of acoustic/elastic phase gradient metasurfaces: Principles, functional elements, tunability, and coding, Appl. Mech. Rev. **74**, 020801 (2022).
10 Y. Li, B. Liang, Z. M. Gu, X. Y. Zou, and J. C. Cheng, Reflected wavefront manipulation based on ultrathin planar acoustic metasurfaces, Sci. Rep. **3**, 2546 (2013).
11 J. Mei, and Y. Wu, Controllable transmission and total reflection through an impedance-matched acoustic metasurface, New J. Phys. **16**, 123007 (2014).
12 Y. Li, X. Jiang, R. Li, B. Liang, X. Zou, L. Yin, and J. Cheng, Experimental realization of full control of reflected waves with subwavelength acoustic metasurfaces, Phys. Rev. Appl. **2**, 064002 (2014).
13 S. W. Fan, S. D. Zhao, A. L. Chen, Y. F. Wang, B. Assouar, and Y. S. Wang, Tunable broadband reflective acoustic metasurface, Phys. Rev. Appl. **11**, 044038 (2019).
14 B. Liu, W. Zhao, and Y. Jiang, Apparent negative reflection with the gradient acoustic metasurface by integrating supercell periodicity into the generalized law of reflection, Sci. Rep. **6**, 38314 (2016).
15 S. Bernard, F. Chikh-Bled, H. Kourchi, F. Chati, and F. Léon, Broadband negative reflection of underwater acoustic waves from a simple metagrating: Modeling and experiment, Phys. Rev. Appl. **17**, 024059 (2022).
16 Y. Li, and B. M. Assouar, Acoustic metasurface-based perfect absorber with deep subwavelength thickness, Appl. Phys. Lett. **108**, 063502 (2016).
17 G. Y. Song, Q. Cheng, T. J. Cui, and Y. Jing, Acoustic planar surface retroreflector, Phys. Rev. Mater. **2**, 065201 (2018).
18 K. F. Graff, Wave Motion in Elastic Solids (Dover Publications, New York, 1991).
19 M. S. Kim, W. R. Lee, Y. Y. Kim, and J. H. Oh, Transmodal elastic metasurface for broad angle total mode conversion, Appl. Phys. Lett. **112**, 241905 (2018).
20 M. S. Kim, W. Lee, C. I. Park, and J. H. Oh, Elastic wave energy entrapment for reflectionless metasurface, Phys. Rev. Appl. **13**, 054036 (2020).
21 Y. Xie, W. Wang, H. Chen, A. Konneker, B. I. Popa, and S. A. Cummer, Wavefront modulation and subwavelength diffractive acoustics with an acoustic metasurface, Nat. Commun. **5**, 5553 (2014).
22 S. Y. Kim, W. Lee, J. S. Lee, and Y. Y. Kim, Longitudinal wave steering using beam-type elastic metagratings, Mech. Syst. Signal Process. **156**, 107688 (2021).
23 J. Mei, L. Fan, and X. Hong, Elastic metagratings with simultaneous highly efficient control over longitudinal and transverse waves for multiple functionalities, Phys. Rev. Appl. **18**, 014002 (2022).
24 S. Y. Kim, Y. B. Oh, J. S. Lee, and Y. Y. Kim, Anomalous mode-converting reflection of elastic waves using strip-type metagratings, Mech. Syst. Signal Process. **186**, 109867 (2023).
25 B. A. Auld, Acoustic Fields and Waves in Solids (John Wiley & Sons, New York, 1973).
26 H. J. Lee, J. R. Lee, S. H. Moon, T. J. Je, E. Jeon, K. Kim, and Y. Y. Kim, Off-centered double-slit metamaterial for elastic wave polarization anomaly, Sci. Rep. **7**, 15378 (2017).
27 B. Ahn, H. J. Lee, and Y. Y. Kim, Topology optimization of anisotropic metamaterials tracing the target EFC and field polarization, Comput. Methods Appl. Mech. Eng. **333**, 176 (2018).
28 M. Zheng, X. Liu, Y. Chen, H. Miao, R. Zhu, and G. Hu, Theory and realization of nonresonant anisotropic singly polarized solids carrying only shear waves, Phys. Rev. Appl. **12**, 014027 (2019).
29 M. Zheng, C. I. Park, X. Liu, R. Zhu, G. Hu, and Y. Y. Kim, Nonresonant metasurface for broadband elastic wave mode splitting, Appl. Phys. Lett. **116**, 171903 (2020).
30 Y. Chen, X. Liu, and G. Hu, Latticed pentamode acoustic cloak, Sci. Rep. **5**, 15745 (2015).

用于宽频完美模态转换和负反射的非谐振弹性超材料

胡洲, 郑明晔, 易凯军, 朱睿, 胡更开

摘要 控制弹性波的反射是非常重要的. 最近, 由广义斯奈尔定律支配的反射型超表面为弹性波的方向和极化控制提供了一个新的自由度. 然而, 反射型超表面的机理是频率相关的, 这大大限制了它们的实际应用. 本文提出了一种与频率无关的超材料, 称为单极化固体(SPS), 用于弹性波的宽带反射控制. 利用设计的单一极化固体实现了完美模式转换, 同时还实现了正反射与负反射之间的切换. 本文开辟了一种宽频弹性波的反射调控的方法, 在结构健康监测、无损检测和弹性波装置方面找到潜在的应用.